Journal of Optics

PAPER

Transverse angular momentum in topological photonic crystals

To cite this article: Wei-Min Deng *et al* 2018 *J. Opt.* **20** 014006

IOP Publishing Journal of Optics
J. Opt. 20 (2018) 014006 (8pp) https://doi.org/10.1088/2040-8986/aa9b06

Transverse angular momentum in topological photonic crystals

Wei-Min Deng, Xiao-Dong Chen, Fu-Li Zhao and Jian-Wen Dong[1]

School of Physics & State Key Laboratory of Optoelectronic Materials and Technologies, Sun Yat-sen University, Guangzhou 510275, People's Republic of China

E-mail: dongjwen@mail.sysu.edu.cn

Received 30 August 2017, revised 9 November 2017
Accepted for publication 16 November 2017
Published 13 December 2017

Abstract

Engineering local angular momentum of structured light fields in real space enables applications in many fields, in particular, the realization of unidirectional robust transport in topological photonic crystals with a non-trivial Berry vortex in momentum space. Here, we show transverse angular momentum modes in silicon topological photonic crystals when considering transverse electric polarization. Excited by a chiral external source with either transverse spin angular momentum or transverse phase vortex, robust light flow propagating along opposite directions is observed in several kinds of sharp-turn interfaces between two topologically-distinct silicon photonic crystals. A transverse orbital angular momentum mode with alternating phase vortex exists at the boundary of two such photonic crystals. In addition, unidirectional transport is robust to the working frequency even when the ring size or location of the pseudo-spin source varies in a certain range, leading to the superiority of the broadband photonic device. These findings enable one to make use of transverse angular momentum, a kind of degree of freedom, to achieve unidirectional robust transport in the telecom region and other potential applications in integrated photonic circuits, such as on-chip robust delay lines.

Keywords: spin-orbit interaction, topological photonics, transverse angular momentum

(Some figures may appear in colour only in the online journal)

1. Introduction

Structured nanoscale light fields have attracted much attention and have brought about many applications, such as the nanometric optical tweezer [1], atomic manipulation [2], quantum communication and information [3]. As structured light fields can carry transverse angular momentum [4–6], e.g. transverse spin angular momentum (TSAM) associated with circular polarization and transverse orbital angular momentum (TOAM) derived from the phase structure of light, one may explore such two important degrees of freedom to achieve unique electromagnetic behaviors and light–matter interaction between structured light fields and nanostructures [7]. One particular example is to employ the angular momentum of structured light fields to excite the valley chiral bulk state in valley photonic crystals [8, 9]. Another issue is to utilize local chirality in the near fields of nanophotonic structures to realize directional photon emission [10, 11]. The discovery of such chiral light–matter interaction brings about the research field of chiral quantum optics [12].

Topological photonics is one of the most promising topics in recent years, with a certain superiority to its predecessor in condensed matter physics, e.g. easy sample preparation and room temperature characterization. Topology degree of freedom in photonics provides a new point of view to mold a robust unidirectional flow of light in various systems [13–33]. However, it brings about a tricky problem in experiments, namely, how to construct a proper pseudo-spin source in different types of photonic systems with time-reversal symmetry protection. In previous literature, several schemes have been proposed to achieve unidirectional transport without backscattering, but they are tough and impractical in the telecom region [17–21]. Compared with pseudo-spin, a true spin, i.e. electric circular

[1] This article belongs to the special issue: Emerging Leaders, which features invited work from the best early-career researchers working within the scope of the *Journal of Optics*. Professor Jian-Wen Dong was selected by the Editorial Board of the *Journal of Optics* as an Emerging Leader.

polarization, is easier to construct in the telecom region. Due to the fact that the optical circularly-polarized source is natural in terms of electric fields, the key point for the excitation of the unidirectional edge state by a true spin is to have a topological photonic crystal of transverse-electric (TE) polarization and to investigate the local chirality of structured light fields inside. Considering that electric circularly-polarized light may carry orbital angular momentum (OAM), a true spin carrying spin and orbital angular momenta will be native for achieving topological functionality on chip-size systems.

In this work, we studied transverse spin and orbital angular momenta in silicon topological photonic crystals when considering TE polarization. By plotting the polarization ellipse of the electric field near the boundary of topological photonic crystals, we found several circular polarization points, of which the handedness is locked to the light propagating direction. Meanwhile, we observed phase vortexes with the handedness locking to the light direction. By exciting transverse spin or the orbital angular momentum mode with different chirality, robust light flow propagating towards the opposite direction was achieved in several kinds of sharp-turn interfaces between two topologically-distinct silicon photonic crystals. Especially, there is a TOAM mode with an alternating phase vortex in the phase distribution of the E_y component. Besides, we also found that the unidirectional light flow is robust to the working frequency even when the ring-size or the position of the pseudo-spin source is changed. By taking advantage of transverse angular momentum, the above findings enable one to realize robust and unidirectional light flow in the telecom region and bring about potential applications in integrated photonic circuits such as on-chip robust delay lines.

2. Topological photonic crystals

Here, we adopt the $\vec{k}\cdot\vec{p}$ method in [34] to derive the Hamiltonian of photonic crystals. A similar Hamiltonian has been studied in TM polarization [19], while we consider TE polarization in this paper. We adopt the definition of TE/TM polarization in a textbook of photonic crystals [35]. So, we have non-zero E_x, E_y and H_z components. For TE-polarized states in two-dimensional photonic crystals, the eigenvalue equation is expressed as

$$-\nabla\cdot\left[\frac{1}{\varepsilon_r(\vec{r})}\nabla H_z\right]=\frac{\omega^2}{c^2}H_z. \tag{1}$$

After applying the Bloch theory, we can express H_z as $H_z(\vec{r})=e^{i\vec{k}\cdot\vec{r}}u(\vec{r})$, where $u(\vec{r})$ is the periodic function. Then equation (1) turns to

$$(\hat{H}_0+\hat{H}_{pert})u(\vec{r})=Eu(\vec{r}), \tag{2}$$

where $\hat{H}_0=-\frac{1}{\varepsilon_r(\vec{r})}\nabla^2-\left[\left(\frac{\partial}{\partial x}\frac{1}{\varepsilon_r(\vec{r})}\right)\cdot\frac{\partial}{\partial x}+\left(\frac{\partial}{\partial y}\frac{1}{\varepsilon_r(\vec{r})}\right)\cdot\frac{\partial}{\partial y}\right]$, $\hat{H}_{pert}=-\frac{2i}{\varepsilon_r(\vec{r})}\vec{k}\cdot\nabla-i\vec{k}\cdot\nabla\frac{1}{\varepsilon_r(\vec{r})}+\frac{k^2}{\varepsilon_r(\vec{r})}$ and $E=\omega^2/c^2$. $\hat{H}_0$ is the unperturbed part and $\hat{H}_{pert}$ is the perturbation part away from the Γ point. Assume there are two pairs of degenerate eigenfunctions at the Γ point, with the eigenvalues being $E_1=E_2$ and $E_3=E_4$. The parity of each eigenfunction is denoted as $f_1=p_x$, $f_2=p_y$, $f_3=d_{x^2-y^2}$, $f_4=d_{2xy}$. Then, on the basis of $[p_x, p_y, d_{x^2-y^2}, d_{2xy}]$, if we consider the perturbation near the Γ point, the Hamiltonian has a 4×4 matrix form

$$\mathbf{H}=\begin{pmatrix}\mathbf{H_{pp}} & \mathbf{H_{pd}}\\ \mathbf{H_{pd}^{\dagger}} & \mathbf{H_{dd}}\end{pmatrix}, \tag{3}$$

where each component is a 2×2 matrix, and † is the conjugate transpose operator. We derived the matrix elements of $\mathbf{H_{pp}}$ by applying second-order degenerate $\vec{k}\cdot\vec{p}$ perturbation theory to the degenerate states f_1 and f_2 [34]. Each component in $\mathbf{H_{pp}}$ is expressed as

$$H_{pp}^{mn}=E_m\delta_{mn}+H'_{mn}+\sum_{\alpha=3,4}\frac{H'_{m\alpha}H'_{\alpha n}}{(E_m-E_\alpha)}, \tag{4}$$

where $m=1,2$, $n=1,2$ and $H'_{mn}=\langle f_m|\,\hat{H}_{pert}|f_n\rangle$. For example, H_{pp}^{11} can be written as

$$\begin{aligned}H_{pp}^{11}&=E_1+\langle f_1|\,\hat{H}_{pert}|f_1\rangle\\&\quad+\sum_{\alpha=3,4}\frac{\langle f_1|\,\hat{H}_{pert}|f_\alpha\rangle\langle f_\alpha|\,\hat{H}_{pert}|f_1\rangle}{E_1-E_\alpha}\\&\approx E_1+q_1k^2+Gk_x^2+Fk_y^2,\end{aligned} \tag{5}$$

where $q_1=|\langle f_1|\,1/\varepsilon_r(\vec{r})|f_1\rangle$, $G=\left(\left|\langle p_x|-\frac{2i}{\varepsilon_r(\vec{r})}\cdot\frac{\partial}{\partial x}|d_{x^2-y^2}\rangle\right|^2-\left|\langle p_x|-i\left(\frac{\partial}{\partial x}\frac{1}{\varepsilon_r(\vec{r})}\right)|d_{x^2-y^2}\rangle\right|^2\right)/(E_1-E_3)$ and $F=\left(\left|\langle p_x|-\frac{2i}{\varepsilon_r(\vec{r})}\cdot\frac{\partial}{\partial y}|d_{2xy}\rangle\right|^2-\left|\langle p_x|-i\left(\frac{\partial}{\partial y}\frac{1}{\varepsilon_r(\vec{r})}\right)|d_{2xy}\rangle\right|^2\right)/(E_1-E_3)$. According to equation (4), we can obtain other components in $\mathbf{H_{pp}}$. Finally, we can express $\mathbf{H_{pp}}$ as

$$\mathbf{H_{pp}}=\begin{pmatrix}E_1+q_1k^2+Gk_x^2+Fk_y^2 & Nk_xk_y\\ Nk_xk_y & E_1+q_2k^2+Fk_x^2+Gk_y^2\end{pmatrix}, \tag{6}$$

where $N\approx F+G$ and $q_2=|\langle f_2|\,1/\varepsilon_r(\vec{r})|f_2\rangle$. In the same way, by applying second-order degenerate $\vec{k}\cdot\vec{p}$ perturbation theory to the degenerate states f_3 and f_4, $\mathbf{H_{dd}}$ can also be obtained and is expressed as

$$\mathbf{H_{dd}}=\begin{pmatrix}E_3+q_3k^2-Gk_x^2-Fk_y^2 & -Nk_xk_y\\ -Nk_xk_y & E_3+q_4k^2-Fk_x^2-Gk_y^2\end{pmatrix}. \tag{7}$$

For non-diagonal terms $\mathbf{H_{pd}}$ and $\mathbf{H_{pd}^{\dagger}}$ in equation (3), these components can be expressed as $H_{pd}^{11}=\langle f_1|\,\hat{H}_{pert}|f_3\rangle=Ak_x$, $H_{pd}^{12}=\langle f_1|\,\hat{H}_{pert}|f_4\rangle\approx Ak_y$, $H_{pd}^{21}=\langle f_2|\,\hat{H}_{pert}|f_3\rangle\approx -Ak_y$, $H_{pd}^{22}=\langle f_2|\,\hat{H}_{pert}|f_4\rangle\approx Ak_x$. The Hamiltonian $\mathbf{H}$ is thus given by

$$\mathbf{H} = \begin{pmatrix} E_1 + q_1k^2 + Gk_x^2 + Fk_y^2 & Nk_xk_y & Ak_x & Ak_y \\ Nk_xk_y & E_1 + q_2k^2 + Fk_x^2 + Gk_y^2 & -Ak_y & Ak_x \\ A^*k_x & -A^*k_y & E_3 + q_3k^2 - Gk_x^2 - Fk_y^2 & -Nk_xk_y \\ A^*k_y & A^*k_x & -Nk_xk_y & E_3 + q_4k^2 - Fk_x^2 - Gk_y^2 \end{pmatrix}, \quad (8)$$

where $q_j = \langle f_j | \, 1/\varepsilon_r(\vec{r}) | f_j \rangle$, $(j = 1,2,3,4)$. Considering that $q_j (j = 1,2,3,4)$ is much smaller than F and G when the degeneration between $[p_x, p_y]$ and $[d_{x^2-y^2}, d_{2xy}]$ is slightly broken, we can neglect the q_j $(j = 1, 2, 3, 4)$ in equation (8). Moreover, if we neglect the second order off-diagonal terms and shift the zero-energy point to $(E_1 + E_3)/2$, the Hamiltonian will be block diagonalized under a new basis of $[p_+, d_+, p_-, d_-]$, where $p_\pm = (p_x \pm ip_y)/\sqrt{2}$ and $d_\pm = (d_{x^2-y^2} \pm id_{2xy})/\sqrt{2}$, yielding

$$\mathbf{H_1} = \begin{pmatrix} M + Bk^2 & Ak_- & 0 & 0 \\ A^*k_+ & -M - Bk^2 & 0 & 0 \\ 0 & 0 & M + Bk^2 & Ak_+ \\ 0 & 0 & A^*k_- & -M - Bk^2 \end{pmatrix}, \quad (9)$$

where $B = (F + G)/2$, $M = (E_1 - E_3)/2$ and $k_\pm = k_x \pm ik_y$. It is interesting to see that the form of equation (9) is similar to the Hamiltonian of the Bernevig–Hughes–Zhang model, implying a topological band gap if the band inversion occurs [36]. Similar to the Bernevig–Hughes–Zhang model, we can evaluate the spin Chern number of the topological photonic crystals as [37]

$$C_\pm = \pm\frac{1}{2}[\mathrm{sgn}(M) + \mathrm{sgn}(-B)]. \quad (10)$$

In equation (10), parameter B is typically negative [38], thus the spin Chern number will be non-zero if the sign of parameter M is positive, namely the frequency of the p states is higher than that of the d states.

To achieve the non-zero spin Chern number, we have to first obtain four specific eigenstates $[p_x, p_y, d_{x^2-y^2}, d_{2xy}]$. Because the on-demand degenerate states are the basis functions of two two-dimensional irreducible representations in the C_{6v} point group, it is straightforward to choose the hexagonal lattice. Note that the hexagonal lattice with a simple unit cell possesses a Dirac cone at the K point, while the selection of the compound unit cell can result in band folding, ensuring the emergence of two sets of degenerate points at the Γ point. In this way, a silicon photonic crystal is designed in a compound unit cell (figure 1(a)) consisting of two types of dielectric rods (blue) embedded in the air background. The two rods have the same permittivity of $\varepsilon_r = 12.08$, while the radii of the center and corner rods are r_1 and r_2, respectively. The distance between the nearest-neighboring rods is $b = a/\sqrt{3}$, where a is the lattice constant. When $r_1 = r_2 = 0.3b$, such silicon photonic crystal has double Dirac cones at the Γ point at the degenerate frequency of 0.799 c/a (figure 1(c)). To break the cone and open a topological gap, we should make the frequency of the p states higher than that of the d states, and it can be achieved when $(r_1, r_2) = (0, 0.33b)$ (figure 1(d)). The highlighted p and d states in figure 1(d) are identified by analyzing the parity of H_z field patterns. In contrast, a trivial gap opens when $(r_1, r_2) = (0.35b, 0.26b)$, as the p states locate below the d states in figure 1(b). Note that these two topologically distinct gaps share a common frequency range, resulting in a characteristic robust edge state at the boundary of such two silicon photonic crystals (figure 2(a)).

3. Transverse angular momentum

In this section, we will demonstrate the transverse spin and orbital angular momenta of topological photonic crystals. The vertical relation between the direction of angular momentum (pink arrow) and the propagating direction (brown arrow) (figure 1(a)) shows the transverse characteristic of angular momentum. In general, one can recombine the in-plane electric fields of the p_x and p_y states when considering the $\pi/2$ rotation in between. For example, we can have an expression with the form of $\frac{i}{\omega\varepsilon_r(\vec{r})}\nabla \times ((p_x \pm ip_y)\hat{z}) = (E_{1x} \mp iE_{1y})(\hat{x} \pm i\hat{y})$ at the unit cell center, where E_{1x} and E_{1y} are the in-plane electric fields of the p_x state, showing that the pseudo-spin states $p_\pm (= (p_x \pm ip_y)/\sqrt{2})$ are of an intrinsic right/left-handed circular polarization. This is verified in a local polarization ellipse map by retrieving the in-plane electric fields of the eigenfunction at the Γ point. It is clear to see in figure 1(e), that the local polarization of the p_x and p_y states is always linear both at and beyond the center of the unit cell (labelled by blue segments in the left column), while the local polarization ellipse of the $p_\pm$ states is indeed electrically circular polarized at the unit cell center (labeled by the blue circle ring in the right column). Note that the local polarization in most of the unit cell is circular or ellipse in the $p_\pm$ states. In other words, the non-zero TSAM density is intrinsic and general in topological photonic crystals.

Note that the p_x and p_y states share the same parities with the two Hermite-Gaussian modes (HG_{10} and HG_{01}), and the latter directly connect to Laguerre–Gaussian modes carrying OAM [39], with the form of $LG_{01} = (HG_{10} + iHG_{01})/\sqrt{2}$ and $LG_{10} = (HG_{10} - iHG_{01})/\sqrt{2}$. Therefore, it is straightforward to expect phase vortexes in the $p_\pm$ states. This is demonstrated by the emergence of the phase vortex, as shown in the left column of figure 1(f). The spiral phase distribution is obvious near the center of the unit cell, but with opposite chirality in the p_+ and p_- states. In addition, it is provable that

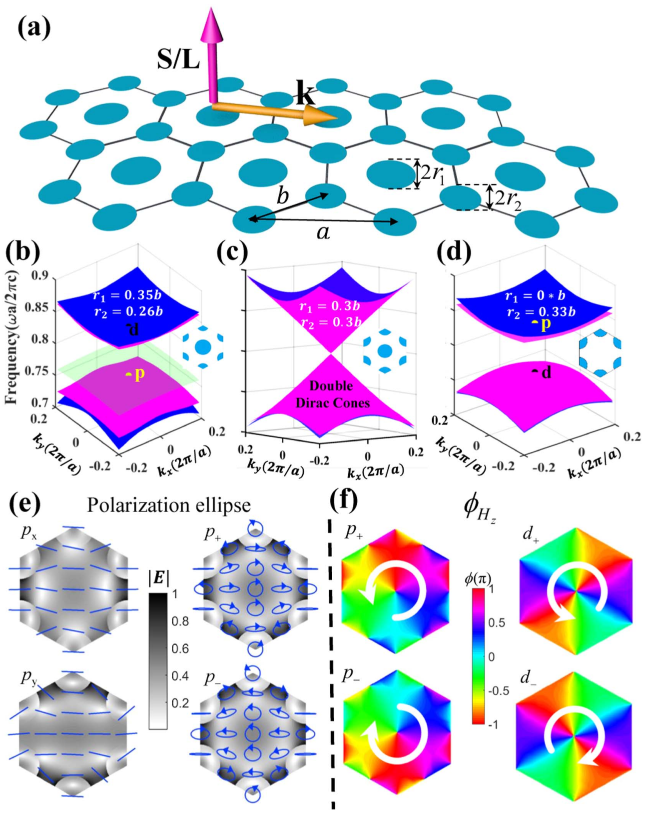

Figure 1. Transverse spin and orbital angular momentum modes in silicon photonic crystals when considering transverse-electric polarization. (a) Hexagonal photonic crystal with a compound unit cell consisting of two dielectric rods (blue) in an air background. The permittivity of the two rods is $\varepsilon_r = 12.08$, while the radii of the center and corner rods are denoted as r_1 and r_2, respectively. The distance between the two rods is $b = a/\sqrt{3}$, where a is the lattice constant. The yellow and pink arrows in (a) indicate the direction of the wave vector and transversely local spin/orbital angular momenta, respectively. (b)–(d) Photonic band structures with various (r_1, r_2) configurations, (b) trivial gap and (0.35b, 0.26b), (c) double Dirac cones and (0.3b, 0.3b), (d) nontrivial gap and (0,0.33b). Note that the double Dirac cones in (c) result from band folding from the zone boundary as the unit cell is chosen to the supercell. (e) Polarization ellipse and (f) phase vortex at the Γ point in the topological photonic crystal with the configuration in (d). Note that such polarization ellipse and phase vortex feature also exist in the trivial crystal in (b).

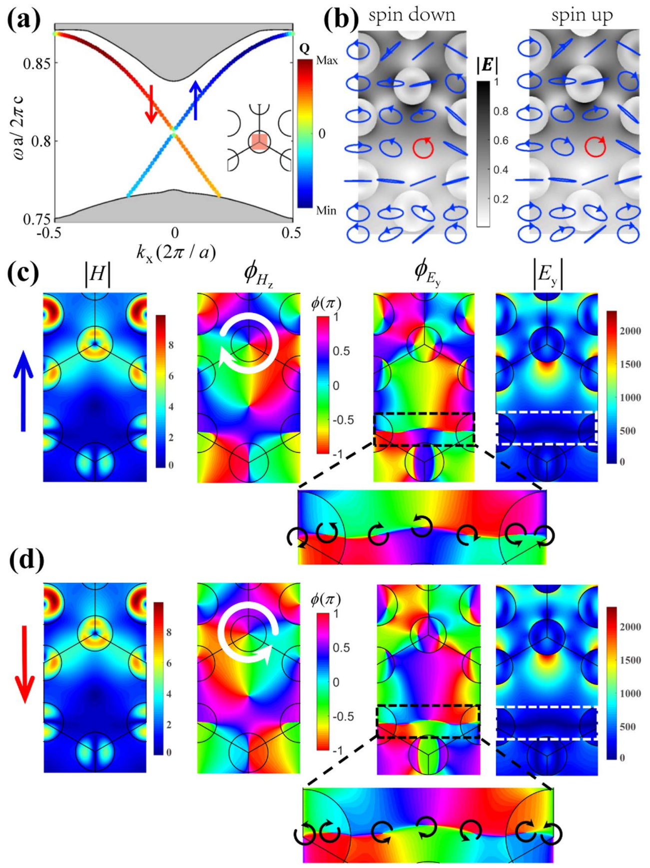

Figure 2. Polarization ellipse and phase vortex at the boundary of the topological photonic crystals. (a) Dispersion relation of the robust edge state spanning within the whole forbidden gap except near the zone center. A vortex factor Q is employed to evaluate the feature of the phase vortex in the pseudo-spin up/down (blue/red) edge states. Positive/negative Q indicates an anti-clockwise/clockwise phase vortex of the H_z field. Inset, the red square is the integration area in the Q calculation. (b) Polarization ellipse distribution when $f = 0.823\ c/a$ and $k_x = \mp 0.08 \times 2\pi/a$, verifying the existence of non-zero transverse spin angular momentum (TSAM) density near the crystal interface. The blue line and circle segments represent various local polarization states at different positions. The background is the magnitude of the normalized electric field. (c)–(d) Magnitude and phase distribution on H_z and E_y components around the crystal interface for the pseudo-spin edge states. The white and black arrows indicate the direction of phase gradient change. The magnified sections show the vortex chain with the alternative phase vortex.

the $d_\pm$ states also carry phase vortexes. This is also consistent with the calculated phase pattern in the right column of figure 1(f).

4. Robust unidirectional propagation by excitation of transverse angular momentum modes

The transverse spin/orbital angular momentum edge mode is crucial for the excitation of robust unidirectional propagation in topological photonic crystals. Figure 2(a) shows the dispersion relation of the edge mode, spanning the whole photonic band gap from the frequency of 0.769 c/a to 0.837 c/a, with the exception of a minigap at the Γ point due to the broken C_{6v} symmetry at the interface. The mode profile (with the frequency of 0.823 c/a) near the boundary between two topologically-distinct photonic crystals is also illustrated in figures 2(b)–(d). For the pseudo-spin up edge state (blue curve in figure 2(a)), one can clearly observe a H_z phase vortex with a clockwise gradient change (white arrow in the second panel of figure 2(c)) and zero H_z intensity at the center (the leftmost panel in figure 2(c)) due to the undefined phase at this singularity point. The pseudo-spin down edge state (red curve in figure 2(a)), which is the time-reversal counterpart of the pseudo-spin up state, has a phase vortex as marked by the counterclockwise white arrow in figure 2(d). In order to quantify such a phase vortex in the whole forbidden gap, a vortex factor $Q = \int_{\text{square}} (\nabla \times \langle \vec{S} \rangle) \cdot d\vec{A}$ is used followed by

[40]. Here, $\langle\vec{S}\rangle$ is the time-averaged Poynting vector, and the integration area is an inscribed square of the dielectric rod possessing the phase vortex. The pseudo-spin edge dispersion in figure 2(a) is then colored by the value of the vortex factor. The vortex factor magnitude reaches a maximum value inside the bandgap while it goes to minimum near either the Brillouin zone center or the upper bandgap boundary due to the spin (vortex) mixture. The sign of the vortex factor, locking to the direction of the local phase vortex in real space, is negative for most of the pseudo-spin up edge states while positive for the time-reversal partner. Note that the group velocity of the pseudo-spin up/down edge state is always positive/negative. One can infer that the sign of the vortex factor is locked to the propagation direction of the light flow. In other words, a phase vortex external source can be utilized to excite the robust unidirectional edge state at the boundary of the topological photonic crystals (to be discussed later).

Alternatively, one can also employ a TSAM source to control the robust unidirectional light flow. Figure 2(b) shows the TSAM mode profile near the edge at the frequency of 0.823 c/a. The polarization ellipse of the electric field is obviously different point-by-point, and some of the positions have chiral electric fields. For example, at the point highlighted in the red circle, it is RCP for the pseudo-spin up edge state while LCP for the pseudo-spin down one. Therefore, a chiral quantum dot placed at the red point may serve as a TSAM source to excite the unidirectional edge state, which is similar to [10] and will be discussed later.

In addition, the two rightmost panels of figures 2(c)–(d) show the E_y fields of the pair of pseudo-spin edge states. A one-dimensional vortex chain can be observed in a near-zero intensity distribution of the E_y field (dashed frame). After labeling the direction of the phase gradient (black arrows in the magnified figures), we further find the alternative sign arrangement of the vortex chain, with a similar feature of the phase structure of propagating beam whose initial phase is of half-integer topological charge [41]. Note that the rotation directions in each vortex are inverse between the two pseudo-spin edge states due to time-reversal-symmetry protection.

Next, we show the angular momenta properties of the bulk and edge modes in topological photonic crystals, by following the formulism in [42]. For the TE mode, the time-averaged energy density and TSAM density can be expressed as $W = (\varepsilon_0\varepsilon_r\,|\vec{E}|^2 + \mu_0\,|\vec{H}|^2)/4$ and $S_z = \mathrm{Im}(E_x^*E_y)\varepsilon_0\varepsilon_r/(2\omega)$, resulting a well-defined normalized TSAM density $\omega S_z/W$. It is obvious that the normalized TSAM density is not only dependent on the polarization of the electric field, but also relates to the time-averaged energy density of the electromagnetic field. For example, a large value of normalized TSAM may result from either circular polarization or small energy density. In contrast, nearly-linear polarization or large energy density can both result in a small value of normalized TSAM. One cannot evaluate the total TSAM quantitatively just from the distribution of polarization ellipse in figure 1(e), while we can from the normalized TSAM density in figure 3(a). More calculations show that the $p_\pm$ states have finite TSAM by

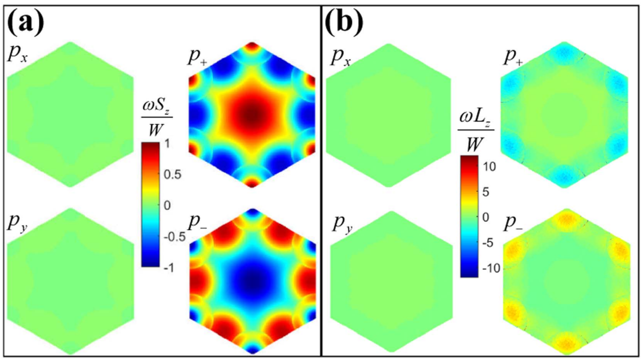

Figure 3. Transverse spin and orbital angular momentum density in silicon photonic crystals when considering transverse-electric (TE) polarization. (a) Transverse spin and (b) transverse orbital angular momentum density distribution at the Γ point in a topological photonic crystal with the configuration in figure 1(d). Here, we use a saturated color bar to show the distribution of transverse orbital angular momentum density in a more obvious way.

non-zero integral TSAM, i.e. $\omega\langle S_z\rangle/\langle W\rangle$, where $\langle ...\rangle$ denotes the surface integration over a unit cell. However, the p_x and p_y states have zero TSAM due to the vanishing integration. In a similar way, the normalized TOAM density can be calculated by the expression of $\omega L_z/W = \omega(\vec{r} - \vec{r}_0) \times \vec{P}/W$, where the momentum density $\vec{P} = Im(\varepsilon_0\varepsilon_r\vec{E}^* \cdot (\nabla)\vec{E} + \mu_0\vec{H}^* \cdot (\nabla)\vec{H})\big/(4\omega)$ and $\vec{r}_0$ is the energy center. Note that the normalized TOAM density includes the contribution from all the components of the electromagnetic field, not just considering only one component. We find that the normalized TOAM density vanishes at the center of the $p_\pm$ states (see the right column of figure 3(b)), although there is a H_z phase vortex around the unit cell center (see the left column of figure 1(f)). Consistent with the total TSAM, the $p_\pm$ states have finite TOAM while the p_x and p_y states have zero TOAM. In addition, the pseudo-spin edge modes still carry both TSAM and TOAM, evaluated by a similar formulism, and the integral region changes to a large-enough mode profile near the interface to ensure numerical convergence.

Exciting robust unidirectional light flow at the boundary of topological photonic crystals needs a source carrying a TSAM or phase vortex. To mimic a phase vortex source, twenty-four equal-amplitude H_z point sources are set isometrically on a circle, named the ring source hereafter. The phase of such a ring source increases clockwise or anti-clockwise with a linear interval of $\pi/12$. Figure 4 plots the topologically-protected results when the radius of the ring source is $R_s = 0.6b$, with the circle center at the white-arrow-surrounding rod in figure 2(c). One can see that the electromagnetic wave propagates in a one-way direction with little reflection, e.g. rightward flow by clockwise phase vortex source excitation in figure 4(a). The excited waves smoothly pass through a series of 60°/120° sharp corners at the boundary of the topological photonic crystal. Moreover, the unidirectional flow has a broadband feature within the whole topological photonic bandgap, see the green curve of figure 5(a). Such unique behavior also occurs when placing a chiral dipole source (i.e. RCP or LCP) at the position with a chiral polarization ellipse

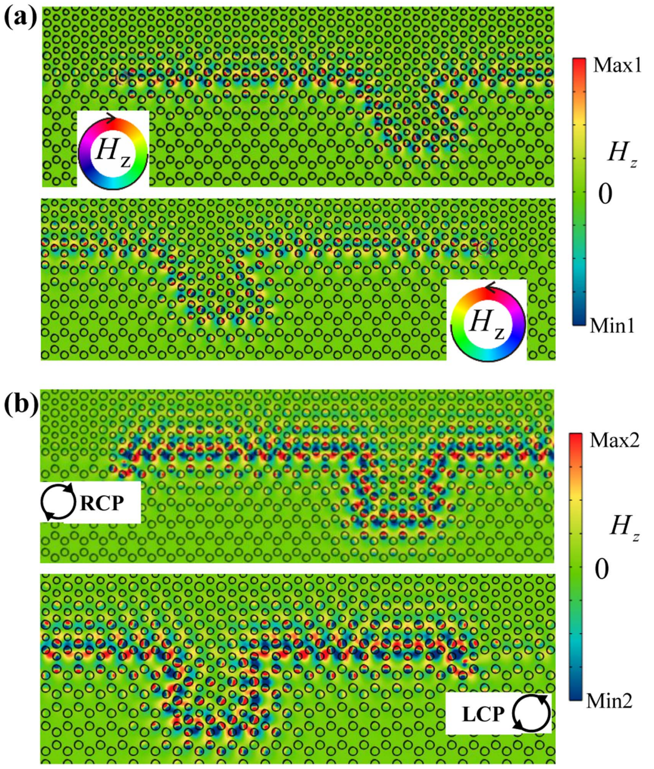

Figure 4. Robust and unidirectional edge states excited by (a) the phase vortex source and (b) TSAM source, with the working frequency of 0.823 c/a. (a) The electromagnetic wave propagates towards the right side and smoothly circumvents a 60° sharp bend with clockwise phase vortex ring source excitation, while it goes leftwards with anti-clockwise phase vortex ring source excitation. Here, the ring source has twenty-four equal-amplitude point sources on a circle with a linear phase interval of $\pi/12$. The semi-diameter of the ring source is 0.6b, and the ring center is at the white-arrow -surrounding rod in figure 2(c). (b) Selective excitation of the robust unidirectional flow by the excitation of the transverse spin angular momentum source. Pseudo-spin up edge state (propagating rightwards) is excited by a RCP source, while pseudo-spin down state (propagating leftwards) by a LCP source. Note that the light flow circumvents the 90° sharp bend, manifesting the diverse design advantage of robust unidirectional flow in future chip-size devices.

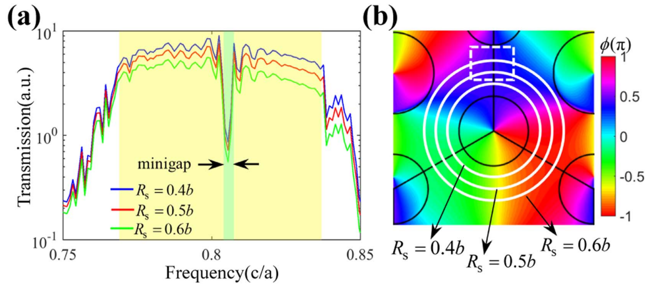

Figure 5. The influence of the ring size on the robust unidirectional flow along the edge with a 60° sharp bend. (a) Transmission spectra excited by a clockwise phase vortex source with a different ring source size of $R_s = 0.4b$ (blue), 0.5b (red) and 0.6b (green), respectively. The yellow region represents the complete common gap and the pale green region represents the minigap. When R_s is tuned from 0.4b to 0.6b, the spectra decrease in the yellow region due to mode mismatch. (b) Phase distribution of H_z eigenfield in pseudo-spin up edge state at the frequency of 0.823 c/a. The radius of three white circles from inner to outer is 0.4b, 0.5b and 0.6b. The dashed rectangle indicates a region where the H_z phase increases anti-clockwise along the white circle, opposite to the phase gradient of the source.

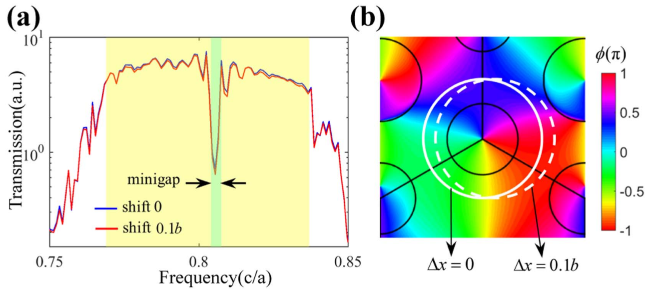

Figure 6. The influence on the same structure and same phase vortex source as those of figure 5, except for a change in the source center location and fixing $R_s = 0.5b$. (a) Transmission spectra with different lateral shift of $\Delta x = 0$ (blue) and $\Delta x = 0.1b$ (red). Note that the two spectra are almost the same in the gap (yellow) region. (b) Phase distribution of H_z eigenfield in pseudo-spin up edge state at the frequency of 0.823 c/a. The solid and dashed circles correspond to a lateral shift of 0 and 0.1b, respectively.

(red in figure 2(b)). Note that the chiral dipole source is used to mimic the TSAM mode, with the phase difference between E_x and E_y of $\pi/2$ and $-\pi/2$, respectively. Note also that we demonstrate a different sharp corner with a 90° bend in figure 4(b), in order to illustrate the diverse design proposals of robust unidirectional flow in future chip-size devices.

Next, we will discuss the transmission spectra of the robust unidirectional flow when we change the size of the ring source and the source position. It is expected that both cases may influence the selective excitation of the robust unidirectional edge state as the local phase vortex is position dependent. The transmission spectra of robust unidirectional flow along the 60° sharp bend is shown in figure 5(a), with same clockwise phase vortex source but different R_s of the ring sources. The yellow background denotes the complete common gap and the green solid rectangle is the minigap. The transmission decreases little with the R_s value from 0.4b (blue) to 0.6b (green), but still maintains a high level in the broadband region, illustrating the predominance of a strong photonic spin–orbit interaction. The small decrease can be understood by comparing the phase gradient of the phase vortex source and the eigenmode. When $R_s = 0.4b$, the phase gradient of the source is consistent with the eigenmode phase, resulting in the best mode match and thus the highest transmission in the complete gap, except for a narrow dip in the minigap (figure 5(a)). However, when R_s increases to 0.5b, a small part of the ring source with a clockwise increasing phase gradient will enter into a dashed region where the eigenmode phase gradient is inversely anti-clockwise. This mode mismatch leads to a slight decrease in the transmission spectra. With R_s further increasing to 0.6b, the more mode mismatch occurs, the further transmission decreases. Figure 6 illustrates the case when the source position has a finite lateral shift while $R_s = 0.5b$

remains unchanged. The nearly same transmission of the two cases indicates that the 0.1*b* shift does not affect the selective excitation, as the phase gradient of the source along the circle still matches the phase gradient in the eigenmode (see the details in figure 6(b)).

Finally, we will briefly discuss three key issues that have to be solved in order to experimentally reproduce the theoretical finding in this work. The first is to design two kinds of photonic crystal slabs which belong to two different topological phases as we discuss in a 2D system. The second is to construct a chiral source to excite the unidirectional edge state. The quantum dot [10] or delicately designed on-chip microdisk [43] can be used to excite the unidirectional edge state. The last is to measure the electromagnetic field above the photonic crystal. This can be accomplished by near-field scanning optical microscope technology [44–46].

5. Conclusion

We revealed the existence of transverse spin and orbital angular momenta in silicon topological photonic crystals by considering TE polarization. The calculated results show non-zero integral TSAM and integral TOAM of pseudo-spin states. Besides, we found a one-dimensional vortex chain with an alternating-sign phase gradient at the boundary of the topological photonic crystals. Taking advantage of transverse spin angular momentum or phase vortex mode with different chirality as the pseudo-spin source, we demonstrated the selective excitation of robust unidirectional light flow along several kinds of sharp bends, manifesting the diverse design advantage of robust unidirectional light flow in future chip-size devices. Moreover, we found that the robustness of the unidirectional light flow can be maintained even when the ring size or position of the source varies in a certain range. Our work paves the way for one to realize robust unidirectional light flow in the telecom region and may bring about some potential applications in integrated photonic circuits such as on-chip robust delay lines. Revealing the local transverse angular momentum in topological photonic crystals may also promote study on the novel phenomenon in classical and quantum optics, especially in the field of chiral quantum optics.

Acknowledgments

This work is supported by the Natural Science Foundation of China (11522437, 61775243, 11704422), Guangdong Natural Science Funds for Distinguished Young Scholar (S2013050015694) and Guangdong Special Support Program.

ORCID iDs

Jian-Wen Dong https://orcid.org/0000-0003-2379-554X

References

[1] Grigorenko A N, Roberts N W, Dickinson M R and Zhang Y 2008 Nanometric optical tweezers based on nanostructured substrates *Nat. Photon.* **2** 365–70
[2] Eigler D M and Schweizer E K 2000 Positioning single atoms with a scanning tunnelling microscope *Nature* **344** 524–6
[3] Mair A, Vaziri A, Weihs G and Zeilinger A 2001 Entanglement of the orbital angular momentum states of photons *Nature* **412** 313–6
[4] Bliokh K Y, Smirnova D and Nori F 2015 Quantum spin Hall effect of light *Science* **348** 1448–51
[5] Bliokh K Y and Nori F 2015 Transverse and longitudinal angular momenta of light *Phys. Rep.* **592** 1–38
[6] Bekshaev A Y, Bliokh K Y and Nori F 2015 Transverse spin and momentum in two-wave interference *Phys. Rev.* X **5** 011039
[7] Bliokh K Y, Rodríguez-Fortuño F J, Nori F and Zayats A V 2015 Spin–orbit interactions of light *Nat. Photon.* **9** 796–808
[8] Dong J-W, Chen X-D, Zhu H, Wang Y and Zhang X 2017 Valley photonic crystals for control of spin and topology *Nat. Mater.* **16** 298–302
[9] Chen X-D, Zhao F-L, Chen M and Dong J-W 2017 Valley-contrasting physics in all-dielectric photonic crystals: orbital angular momentum and topological propagation *Phys. Rev.* B **96** 020202
[10] Sollner I *et al* 2015 Deterministic photon-emitter coupling in chiral photonic circuits *Nat. Nanotechnol.* **10** 775–8
[11] Young A B, Thijssen A C, Beggs D M, Androvitsaneas P, Kuipers L, Rarity J G, Hughes S and Oulton R 2015 Polarization engineering in photonic crystal waveguides for spin-photon entanglers *Phys. Rev. Lett.* **115** 153901
[12] Lodahl P, Mahmoodian S, Stobbe S, Rauschenbeutel A, Schneeweiss P, Volz J, Pichler H and Zoller P 2017 Chiral quantum optics *Nature* **541** 473–80
[13] Wang Z, Chong Y, Joannopoulos J D and Soljačić M 2008 Reflection-free one-way edge modes in a gyromagnetic photonic crystal *Phys. Rev. Lett.* **100** 013905
[14] Poo Y, Wu R-X, Lin Z, Yang Y and Chan C T 2011 Experimental realization of self-guiding unidirectional electromagnetic edge states *Phys. Rev. Lett.* **106** 093903
[15] Wang Z, Chong Y, Joannopoulos J and Soljačić M 2009 Observation of unidirectional backscattering-immune topological electromagnetic states *Nature* **461** 772–5
[16] Fang K, Yu Z and Fan S 2012 Realizing effective magnetic field for photons by controlling the phase of dynamic modulation *Nat. Photon.* **6** 782–7
[17] Khanikaev A B, Mousavi S H, Tse W-K, Kargarian M, MacDonald A H and Shvets G 2013 Photonic topological insulators *Nat. Mater.* **12** 233–9
[18] Chen W-J, Jiang S-J, Chen X-D, Zhu B, Zhou L, Dong J-W and Chan C T 2014 Experimental realization of photonic topological insulator in a uniaxial metacrystal waveguide *Nat. Commun.* **5** 5782–8
[19] Wu L-H and Hu X 2015 Scheme for achieving a topological photonic crystal by using dielectric material *Phys. Rev. Lett.* **114** 223901
[20] Xiao B, Lai K, Yu Y, Ma T, Shvets G and Anlage S M 2016 Exciting reflectionless unidirectional edge modes in a reciprocal photonic topological insulator medium *Phys. Rev.* B **94** 195427
[21] Yang Y, Xu Y, Xu T, Wang H, Jiang J, Hu X and Hang Z 2016 Visualization of unidirectional optical waveguide using topological photonic crystals made of dielectric material arXiv:1610.07780
[22] Hafezi M, Mittal S, Fan J, Migdall A and Taylor J M 2013 Imaging topological edge states in silicon photonics *Nat. Photon.* **7** 1001–5

[23] Rechtsman M C, Zeuner J M, Plotnik Y, Lumer Y, Podolsky D, Dreisow F, Nolte S, Segev M and Szameit A 2013 Photonic Floquet topological insulators *Nature* **496** 196–200
[24] Tan W, Sun Y, Chen H and Shen S Q 2014 Photonic simulation of topological excitations in metamaterials *Sci. Rep.* **4** 3842–8
[25] Chen X-D, Deng Z-L, Chen W-J, Wang J-R and Dong J-W 2015 Manipulating pseudospin-polarized state of light in dispersion-immune photonic topological metacrystals *Phys. Rev.* B **92** 014210
[26] Gao W, Lawrence M, Yang B, Liu F, Fang F, Beri B, Li J and Zhang S 2015 Topological photonic phase in chiral hyperbolic metamaterials *Phys. Rev. Lett.* **114** 037402–6
[27] Lu L, Wang Z, Ye D, Ran L, Fu L, Joannopoulos J D and Soljačić M 2015 Experimental observation of Weyl points *Science* **349** 622–4
[28] Cheng X, Jouvaud C, Ni X, Mousavi S H, Genack A Z and Khanikaev A B 2016 Robust reconfigurable electromagnetic pathways within a photonic topological insulator *Nat. Mater.* **15** 542–8
[29] Gao F *et al* 2016 Probing topological protection using a designer surface plasmon structure *Nat. Commun.* **7** 11619
[30] He C, Sun X, Liu X, Lu M, Chen Y, Feng L and Chen Y 2016 Photonic topological insulator with broken time-reversal symmetry *Proc. Natl Acad. Sci.* **113** 4924–8
[31] Lu L, Fang C, Fu L, Johnson S G, Joannopoulos J D and Soljačić M 2016 Symmetry-protected topological photonic crystal in three dimensions *Nat. Phys.* **12** 337–40
[32] Shalaev M I, Desnavi S, Walasik W and Litchinitser N M 2017 Reconfigurable topological photonic crystal arXiv:1706.05325
[33] Weimann S, Kremer M, Plotnik Y, Lumer Y, Nolte S, Makris K G, Segev M, Rechtsman M C and Szameit A 2017 Topologically protected bound states in photonic parity-time-symmetric crystals *Nat. Mater.* **16** 433–8
[34] Mildred S D, Gene D and Jorio A 2008 *Group Theory: Application to the Physics of Condensed Matter* 1st edn (Berlin: Springer)
[35] Joannopoulos J D, Johnson S G, Winn J N and Meade R D 2008 *Photonic Crystals: Molding the Flow of Light* 2nd edn (Princeton, NJ: Princeton University Press)
[36] Bernevig B A, Hughes T L and Zhang S-C 2006 Quantum spin Hall effect and topological phase transition in HgTe quantum wells *Science* **314** 1757–61
[37] Shen S-Q 2012 *Topological Insulators: Dirac Equation in Condensed Matters* (*Springer Series in Solid-State Sciences* vol 174) 1st edn (Berlin: Springer)
[38] Mei J, Chen Z and Wu Y 2016 Pseudo-time-reversal symmetry and topological edge states in two-dimensional acoustic crystals *Sci. Rep.* **6** 32752
[39] Allen L, Beijersbergen M W, Spreeuw R and Woerdman J 1992 Orbital angular momentum of light and the transformation of Laguerre–Gaussian laser modes *Phys. Rev.* A **45** 8185–9
[40] Lu J, Qiu C, Ke M and Liu Z 2016 Valley vortex states in sonic crystals *Phys. Rev. Lett.* **116** 093901
[41] Leach J, Yao E and Padgett M J 2004 Observation of the vortex structure of a non-integer vortex beam *New J. Phys.* **6** 71
[42] Bliokh K Y, Bekshaev A Y and Nori F 2017 Optical momentum, spin, and angular momentum in dispersive media *Phys. Rev. Lett.* **119** 073901
[43] Rodríguez-Fortuño F J, Barber-Sanz I, Puerto D, Griol A and Martínez A 2014 Resolving light handedness with an on-chip silicon microdisk *ACS Photonics* **1** 762–7
[44] Burresi M, Engelen R J, Opheij A, van Oosten D, Mori D, Baba T and Kuipers L 2009 Observation of polarization singularities at the nanoscale *Phys. Rev. Lett.* **102** 033902
[45] Rotenberg N and Kuipers L 2014 Mapping nanoscale light fields *Nat. Photon.* **8** 919–26
[46] De Angelis L, Alpeggiani F, Di Falco A and Kuipers L 2016 Spatial distribution of phase singularities in optical random vector waves *Phys. Rev. Lett.* **117** 093901